

**Title page**

**Title:** Time-scales of Radio Emission in PSR J0437-4715 at 327 MHz  
**Short title:** Time-scales in PSR J0437-4715  
**Name:** M. Vivekanand  
**Address:** National Center for Radio Astrophysics  
Tata Institute of Fundamental Research  
Pune University Campus, P. O. Box 3  
Ganeshkhind, Pune 411007  
India.  
**Email:** vivek@ncra.tifr.res.in  
**Status:** Accepted for publication in Vol 543 (1 Nov 2000) of *The Astrophysical Journal*

# Time-scales of Radio Emission in PSR J0437-4715 at 327 MHz

M. Vivekanand

National Center for Radio Astrophysics, Tata Institute of Fundamental Research, Pune University Campus, P. O. Box 3, Ganeshkhind, Pune 411007, India.

## ABSTRACT

Time-scales of radio emission are studied in PSR J0437-4715 at 327 MHz using almost half a million periods of high quality data from Ooty Radio Telescope. The radio emission in this milli second pulsar occurs on a short ( $s$ ) time-scale of  $\approx 0.026 \pm 0.001$  periods, and on a ( $l$ ) time-scale that is much longer than the widths of the components of the integrated profile ( $\approx 0.05$  periods). The width of the  $s$  emission increases with its increasing relative contribution to the total radio emission. This may provide constraints for the details of discharge of vacuum gaps above pulsar polar caps. The  $s$  emission occasionally takes place in the form of intense spikes, which are confined to the main component of the integrated profile for 90% of the time. The positions of spikes within a component of the integrated profile have no simple relation to the shape of that component. This may have impact on the interpretation of the integrated profile components in terms of independent regions of emission on the polar cap.

*Subject headings:* Pulsars general: stars, radio, time-scales of radio emission, Pulsars individual: PSR J0437-4715, PSR B0950+08, PSR B0031-07

## 1. Introduction

While it is becoming clear that the radio emission properties of normal and milli second (ms) pulsars are broadly similar (Gil & Krawczyk 1997; Jenet et al 1998; Kramer et al 1999), it is not yet clear exactly how similar they are. This is an important issue because of the three to four orders of magnitude difference in their periods and period derivatives. That a similar radio emission mechanism operates over such a wide range of the two most fundamental parameters of pulsars, is probably an important clue to the as yet unsolved problem of pulsar radio emission mechanism.

This issue has been difficult to resolve since the radio emission from ms pulsars is very weak in comparison to that from normal pulsars, which are themselves considered weak radio emitters among cosmic sources. While several normal pulsars have been well studied for the details of their radio emission (see Manchester & Taylor 1977), among ms pulsars PSR J0437-4715 is one of the few that are bright enough for such detailed studies (McConnell et al 1996; Ables et al 1997 (paper I); Navarro et al 1997; Jenet et al 1998; Vivekanand et al 1998 (paper II)). This is the third paper in the series which discusses radio observations of PSR J0437-4715 at 327 MHz using Ooty Radio Telescope (ORT), which has only a single polarization. This pulsar has a rotation period of  $\approx 5.757$  ms and is in a binary system of orbital period  $\approx 5.74$  days. It is known to have radio emission in two modes – one over times scales of  $\approx 0.01$  periods, and the other over  $\approx 0.1$  to 0.5 periods. Paper I discussed one particular aspect of the former emission (spiky), while paper II discussed the overall properties of PSR J0437-4715. Jenet et al 1998 study this pulsar in detail at  $\approx 1400$  MHz. This paper studies the time scales of radio emission in PSR J0437-4715 at 327 MHz, using the auto-correlation function (ACF).

Attempts have been made to model the integrated profile of PSR J0437-4715 into independent components of emission (Gil & Krawczyk 1997). In this paper the time-scales of radio emission are studied in the entire period, as well as in three major components of emission in the integrated profile; they are modeled as the Gaussian shown in Figure 1. The analysis was repeated for each of the three components by multiplying the flux density in each period by the Gaussian of the corresponding component. The ACF is independent of the amplitudes of the components.

## 2. Auto-Correlation Function (ACF)

The details of data acquisition and pre-analysis are described in papers I and II. Briefly, ORT was used to obtain 436,500 periods of high quality data on PSR J0437-4715, sampled at 0.1024 ms. The data were collected in 36 files each containing 12,125 useful periods of continuous data (paper II analyzed 34 of these files). Since the pulsar’s rotation period is continuously Doppler shifted, the data was re-sampled at  $\approx 0.1028$  ms, depending upon the average period of the pulsar in each file, so that there are exactly 56 time samples in each period. The data in each file were shifted so that all 36 integrated profiles were aligned, correct to half a sample. Thus the radio emission properties can be studied as a function of “phase” or “longitude” within each period, across all files (Vivekanand et al 1998).

Figures 2 and 3 describe the method of obtaining the time scales of radio emission in PSR J0437-4715. First, the data of each period were centered in an array of length

64 samples (top frame of Figure 2). Then they were auto-correlated after weighting by a Hamming function. The resulting ACF is shown in the bottom frame of Figure 2, as a function of the time delay  $t$ . Since the ACF is an even function of  $t$ , it was fit to a curve of the form

$$\text{ACF} = k_0 + k_1 t^2 + \sum_{i=1}^{N_g} a_i \exp - \left[ \frac{t}{b_i} \right]^2. \quad (1)$$

The analysis used routines from Numerical Recipes (Press et al 1989), after modifying and debugging them for double precision arithmetic. The ACF for each of the 436,500 periods was fit to four variations of equation 1:  $N_g = 2$  and  $N_g = 3$ , each of which without and with the quadratic term  $k_1$ . This was found sufficient to model more than 75% of the data.

For each of the four variations, the parameters of the fit were constrained as follows (provided that the basic non-linear fit converged): (1) The root mean square (rms) error  $\sigma_f$  on any parameter  $f$  in equation 1 should be less than 1.0 fractionally, i.e.,  $\sigma_f/f < 1.0$ ; (2) The amplitudes  $a$  of the Gaussian should be positive, otherwise the derived time-scale will not make sense, and should be less than  $1.0 + \sigma_a$  (since the peak of the ACF is normalized to 1.0 by definition); (3) For the same reason, the estimated value of the ACF at  $t = 0.0$ , which is  $k_0 + \sum_{i=1}^{N_g} a_i$ , must be equal to 1.0, consistent with its rms error; (4) The absolute value of the coefficient  $k_0$  must be less than 0.1; and (5) The term  $|k_1 t^2|$  must not contribute more than 0.1 (in magnitude) to the ACF at the extreme values of the abscissa ( $t = \pm 0.5174$  periods) in the bottom frame of Figure 2.

For each value of  $N_g$ , the results of the corresponding two variations (without and with  $k_1$ ) were combined in the following manner: (1) When neither variation was able to fit the ACF, that period was set aside for later fitting, or given up altogether; (2) When only one variation fit the ACF, that solution was adopted; (3) When both variations fit the ACF, the following was done:

- The Gaussian were sorted in the increasing order of width ( $b$ ) for proper comparison between the two variations.
- All parameters except  $k_1$  in equation 1 were checked for consistency between the two variations, by the formula

$$\left| \frac{f_1 - f_2}{\sqrt{\sigma_{f_1}^2 + \sigma_{f_2}^2}} \right| < 3.0. \quad (2)$$

where the subscripts 1 and 2 refer to the above two variations, respectively.

- If all above parameters were consistent in the two variations, then the results with  $k_1$  fitted were chosen if  $k_1$  was significant ( $\sigma_{k_1}/k_1 < 1.0$ ); otherwise the results without  $k_1$  fitted were chosen.
- If even one of the above parameters was inconsistent in the two variations, then the results with the lower  $\chi^2$  were chosen, by using equation 2 with  $f$  replaced by  $\chi^2$ , and with 3.0 replaced by 2.0. A minimum  $\chi^2$  criterion should be applied with caution in this problem, because of fits such as that in Figure 3, which are considered good for obtaining the time-scale of emission, although the  $\chi^2$  is high.

The results with  $N_g = 3$  were utilized for only those periods that could not be fit with  $N_g = 2$ . Finally, only those results were retained whose  $\chi^2$  deviated from the mean value in each file by less than three standard deviations.

## 2.1. Discussion of the Model Fits

The best fit parameters for the ACF in Figure 2 are:  $N_g = 2$ ,  $a_1 = 0.2541 \pm 0.0031$ ,  $b_1 = 0.0297 \pm 0.0005$ ,  $a_2 = 0.8190 \pm 0.0037$ ,  $b_2 = 0.2049 \pm 0.0010$ ,  $k_0 = -0.0728 \pm 0.0041$ ,  $k_1 = 0.2509 \pm 0.0314$ , the rms deviation of the ACF about the fitted curve being 0.0138. The rms errors were obtained in the usual manner using the covariance matrix, the rms deviation of the ACF, and the number of degrees of freedom. The best fit parameters in Figure 3 are:  $N_g = 2$ ,  $a_1 = 0.5117 \pm 0.0109$ ,  $b_1 = 0.0159 \pm 0.0005$ ,  $a_2 = 0.5068 \pm 0.0054$ ,  $b_2 = 0.2366 \pm 0.0035$ ,  $k_0 = -0.0171 \pm 0.0037$ ,  $k_1$  not being fit, the rms deviation of the ACF being 0.0504. The latter rms deviation is significantly higher due to the double pulsed structure in the top frame of Figure 3, which creates the symmetric peaks in the ACF at around  $t = \pm 0.1$  periods in the bottom frame, which are fit only in a mean sense. This will slightly over estimate the width  $b_2$  for the wider component of the ACF.

The above analysis fitted 81.54% of the periods without any component weighting, and 76.69%, 84.66% and 76.00% of the periods in the three components of the integrated profile in Figure 1, respectively. This was considered sufficient because of the extremely large number of periods available (436,500) to begin with. The majority of the periods required only two time-scales of emission for proper representation; the fraction of the fitted periods that required  $N_g = 3$  was 0.24%, 10.91%, 1.25% and 1.67% in the above four cases, respectively.

It is not possible to visually compare the curve fits with the computed ACF for all periods. This was done for 4800 randomly chosen periods, or  $\approx 1.1\%$  of the total periods.

In addition, 20 periods having the lowest  $\chi^2$  and 20 periods having the highest  $\chi^2$  were also examined visually in four of the 36 data files (that were also chosen randomly). Only one or two fits were found to be unsatisfactory. Assuming that this number is 3, the maximum fraction of misfit periods one expects is  $3/4800 \approx 0.0063\%$ . However fluctuations in this fraction will lead to a maximum fraction of misfit periods of  $(3 + 5 \times \sqrt{3})/4800 \approx 0.24\%$ , at the five standard deviation confidence level; this takes into account the fact that only  $\approx 1.1\%$  of the total number of periods were tested. This is unlikely to influence the results of this paper. This random checking was repeated for each of the three components of the integrated profile in Figure 1, with similar results.

### 3. Duration of Time-Scales

Figure 4 shows the normalized probability density  $p(a, b)$  of occurrence of  $a$  and  $b$  for the entire integrated profile and for the three components of the integrated profile in Figure 1. The estimated values of  $a$  (or  $b$ ) were assumed to be Gaussian random variables with standard deviation  $\sigma_a$  (or  $\sigma_b$ ), which are the rms errors obtained by curve fitting the ACF. Assuming that the errors  $\sigma_a$  and  $\sigma_b$  are uncorrelated,  $p(a, b)$  can be defined as

$$\begin{aligned}
 p(a, b) = & \frac{1}{2\pi N_P} \sum_{i=1}^{N_P} \\
 & \left[ \frac{1}{\sigma_{a_s} \sigma_{b_s}} \exp - \left\{ \left( \frac{a - a_s}{\sigma_{a_s}} \right)^2 + \left( \frac{b - b_s}{\sigma_{b_s}} \right)^2 \right\} \right]_i \\
 & + \left[ \frac{1}{\sigma_{a_l} \sigma_{b_l}} \exp - \left\{ \left( \frac{a - a_l}{\sigma_{a_l}} \right)^2 + \left( \frac{b - b_l}{\sigma_{b_l}} \right)^2 \right\} \right]_i
 \end{aligned} \tag{3}$$

where the subscripts  $s$  and  $l$  refer to small and large time-scales, respectively, and the sum is taken over all valid periods  $N_P$ . The distribution of the third time-scale is similar to that of  $l$ , and they are insignificant in number anyway; so they have not been plotted in Figure 4. Note that any correlation observed in the function  $p(a, b)$  refers to that between the mean values of  $a_s$  and  $b_s$ , or  $a_l$  and  $b_l$ .

Table 1 shows the mean values of the widths  $b$  of the above three time-scales, estimated in the four plots of Figure 4. The rms errors for the third time-scale are significantly higher than the rest because of the much smaller numbers. It is easy to verify that the longer time-scales ( $l$  and 3) scale roughly as the width of the corresponding component

of the integrated profile, while the shorter time-scale ( $s$ ) is almost constant in the three components.

The amplitudes  $a$  of the  $s$  and  $l$  time-scales are anti-correlated with each other; this is expected since the peak ACF is normalized to 1.0, and the third time-scale contributes insignificantly to the ACF. The amplitudes  $a$  are a rough measure of the relative energy in those time-scales. It is difficult to obtain from them the exact energy in each time-scale of emission in PSR J0437-4715, due to the behavior of the ACF as in Figure 3.

Further, the amplitudes  $a$  and widths  $b$  are correlated for the short time-scale ( $s$ ) emission, while they are not correlated for the long time-scale ( $l$ ) emission. This is evident in all four plots of Figure 4. To study this quantitatively, horizontal cuts were taken in plots (a) and (c) of Figure 4, the former for the mean effect, and the latter for the maximum effect. The  $p(a, b)$  cut at each  $a$  was modeled as two Gaussian, to represent the two time-scales. The positions  $\langle b \rangle$  of these Gaussian were fit to a straight line as a function of  $a$  (these are shown in Figures 4a and 4c):

$$\langle b \rangle = \alpha + \beta a. \quad (4)$$

In Figure 4a,  $\alpha = 0.0175 \pm 0.0002$  and  $\beta = 0.0135 \pm 0.0005$  for the  $s$  emission, while  $\alpha = 0.2129 \pm 0.0027$  and  $\beta = 0.0060 \pm 0.0040$  for the  $l$  emission. The corresponding numbers in Figure 4c are  $\alpha = 0.0189 \pm 0.0004$  and  $\beta = 0.0159 \pm 0.0008$  for the  $s$  emission, and  $\alpha = 0.0621 \pm 0.0005$  and  $\beta = -0.0023 \pm 0.0009$  for the  $l$  emission. In both plots  $\beta$  is much larger for the  $s$  emission than for the  $l$  emission, for which it is almost negligible; it is also much more significant relative to its rms error. This verifies the above claim.

An alternate fit was also tried by incorporating a quadratic term  $\gamma a^2$  into equation 4. For the  $s$  emission the earlier trend was verified, while for the  $l$  emission it gave a curvature in the opposite sense, which is also obvious by visual inspection of Figure 4. It may be tempting to claim here that the  $a$  and  $b$  for the  $l$  emission are actually anti-correlated. However, this could also be due to the fact that our curve fitting to the ACF gave biased (higher) values of  $b$  in data such as that shown in Figure 3; and this effect appears to be larger for lower  $a$  (i.e., for weaker  $l$  emission). Therefore the possible anti-correlation of  $a$  and  $b$  in the  $l$  emission has to be justified with better data or with more sophisticated analysis. Note that such a problem does not occur for the  $s$  emission.

The trend seen in Figure 4 was noticed in all 36 individual files of data. It was verified visually for some of the strongest “spikes” of radio emission. It is also consistent with the claim of Jenet et al 1998 that they “observe a significant inverse correlation between pulse peak and width” for the spiky emission (see below). Therefore this appears to be a genuine

feature of radio emission in PSR J0437-4715. This result is also independent of the type A and type B integrated profiles discussed in Figure 8 of Vivekanand et al 1998.

#### 4. Distribution of Spikes

Ables et al 1997 studied the distribution of the spiky emission from PSR J0437-4715 in the “phase” or “longitude” space. They claim that “The spikes are observed almost exclusively in a  $10^\circ$  phase window centered on the main pulse. Within that window the phase distribution has a periodic variation”. The latter claim has been found invalid by Jenet et al 1998. Ables et al 1997 claimed a very high resolution in the phase space; this section attempts a more modest (and probably what should have been the more preliminary) study of the problem.

The method of analysis is similar to that described earlier, except that (1) only those periods were chosen which had flux density peaks higher than a threshold value of 10.0 (in arbitrary units) in the data file with the highest average energy per time sample  $\langle E \rangle_m = 0.6622$ ; for any other file the threshold was determined by  $10.0 \times \langle E \rangle / \langle E \rangle_m$ ; (2) the curve fitting was done to the flux density of the highest peak and not to the ACF (i.e., to the top frame in Figures 2 and 3); and (3) the position of the peak was also fit. This was done for components 1 and 2 of the integrated profile, with the following threshold values for the most luminous data file: 7.5, 10.0, 12.5 and 15.0 (at this level of threshold, no spikes were found in component 3). About 90% of the spikes occurred in component 2, in which the number of periods with spikes above the four thresholds were 10,853, 2735, 800 and 222, respectively. This implies that the probability of occurrence of spikes decreases  $\approx$  exponentially with their peak flux density. This result also holds for component 1.

Figure 5 shows the probability distribution of the peak flux densities and positions of the spikes in component 2; the technique is similar to that used in obtaining Figure 4, where one assumed the abscissa and the ordinate to be distributed as Gaussian random variables. Integrating this plot vertically one obtains the probability distribution of the positions of the spikes within component 2. Comparing this with the component 2 profile in Figure 1, it is clear that the probability of occurrence of the spikes in pulsar rotation “phase” is not simply related to the shape of the integrated profile in that range of phase. It is also not simply related to the integrated profile formed by the spikes alone, which is only marginally different from Figure 1. By visual inspection it appears that this distribution can be modeled in several ways, including possibly as a Gaussian like peak on top of a plateau that is tapering down towards increasing abscissa. It is probably wise to await more



or better data before doing rigorous curve fitting to this probability distribution.

Figure 6 shows the same information for spikes occurring in component 1 of the integrated profile; the probability distribution looks similar to that in Figure 5, except that it is much more noisy, since it contains 303 periods only. These results are independent of the type A and type B integrated profiles discussed in Figure 8 of Vivekanand et al 1998.

This section can not comment on the veracity of the Ables et al 1998 result that has been contested, since the technique used here can not achieve the phase resolution claimed by them. The phase resolution here is determined by the rms errors obtained by the curve fitting procedure.

Figure 7 shows the probability of occurrence of the peak fluxes and widths of the spikes in component 2 of the integrated profile; it verifies the inverse correlation seen in Figure 8 of Jenet et al 1998 (which, the reader is reminded, was observed at  $\approx 1400$  MHz). However, Figure 7 also shows that the average energy in a spike is an increasing function of the width, consistent with the results of Figure 4. This implies that the inverse correlation between peak fluxes and widths is such that their product shows a positive correlation.

## 5. Discussion

First, one will compare the results on PSR J0437-4715 obtained by Jenet et al 1998 at 1380 MHz, and by Vivekanand et al 1998 (paper II) and this work at 327 MHz. The former use coherent dedispersion to obtain a typical time resolution of  $2.56 \mu$  sec, with dispersion smearing of  $3.26 \mu$  sec, while the latter have a time resolution of  $102.8 \mu$  sec, which is several times worse. The former conclude that PSR J0437-4715 shows neither systematic drifting sub-pulses nor the nulling phenomenon at 1380 MHz, and note the broad spectral feature in the fluctuation spectrum. The latter confirm these results at 327 MHz, and study them in much greater detail. The former do not test for long time scale (of the order of several tens or hundreds of periods or more) flux variations, while the latter show that PSR J0437-4715 has such flux variations at 327 MHz, although this must be verified with full polarization data. The pulse energy distributions are similar at both radio frequencies, with the conclusion that there are no giant pulses in PSR J0437-4715. Both works conclude that there is no emission in PSR J0437-4715 at very short time scales, which is canonically known as “micro-structure” in pulsars; in this regard the current work is limited by the relatively large sampling interval. The former show that the quasi periodic phase modulation of the spiky emission in PSR J0437-4715, that was claimed by Ables et al 1997 (paper I), does not exist at 1380 MHz; the latter do not have the time resolution

to verify this. The former show that the peak fluxes of the spikes are anti-correlated with their widths; the latter confirm this. Based on this the former claim that the pulse energies are more or less constant, while the latter show that they are positively correlated with the pulse widths.

The spiky emission of PSR J0437-4715 must be studied keeping in mind the giant pulse phenomenon observed in the ms pulsar PSR B1937 +21 (Sallmen & Backer 1995), and the normal Crab pulsar. Until all radio pulsars within a period range are studied systematically for spiky emission, which has probably not occurred so far, it is not possible to claim whether the rotation period is the main parameter that determines the spiky emission from radio pulsars. Such an exercise will also throw light on whether the low period (0.253 s) but normal pulsar PSR B0950+08, that is known to have impulsive emission (Manchester & Taylor 1977), falls roughly in the same category as PSR J0437-4715.

The time-scale of the  $l$  emission is expected to roughly scale as the width of the component of the integrated profile that it occurs in, due to the multiplication by the corresponding Gaussian before the ACF is computed, if it is a genuinely long time-scale emission, much longer than the widths of the components. Conversely, the width of the  $s$  emission is expected to be independent of the component widths if it is much smaller than them. The actual time-scale of the  $s$  emission is unlikely to be shorter than that mentioned in Table 1 because of the sampling interval (0.1024 ms) of this data (Jenet et al 1998).

The result that the  $s$  time-scale is an increasing function of its relative contribution to the integrated flux density, should be contrasted with the behavior reported in normal pulsars (Manchester & Taylor 1977), as well as in PSR J0437-4715 itself, where the peaks of the sub-pulses are anti-correlated with their widths. At first glance the latter result might imply that the integrated fluxes of sub-pulses are roughly independent of their widths, which is not true at least in PSR J0437-4715. So it is important not to conclude one from the other. To the best of this author’s knowledge Figure 4 has not been estimated for sub-pulses of normal pulsars. Two points need to be clarified here. First, the spikes reported here have widths (in “phase” space) comparable to those of sub-pulses in normal pulsars, and not those of micro-structure (also see Jenet et al 1998). Second, the above comparison is justified only if the “relative contribution to the integrated flux” also implies the “integrated flux” in the average sense, which is expected from a statistical viewpoint unless correlations are observed to the contrary. Further, the visual inspection mentioned earlier, as well as Figure 7, confirms such conjecture.

It will be interesting to verify Figure 4 of this paper in the data of Jenet et al 1998. If verified, the positive correlation between the energies and widths of the spikes would be a

broad band phenomenon, which behaves more like micro-structure, rather than sub-pulses in normal pulsars!

The above might have important implications for the details of the discharge of the vacuum gap above pulsar polar caps (Ruderman & Sutherland 1975). Let us assume that the basic pulsar radio emission occurs in terms of sparks, and several contiguous sparks make a sub-pulse. If the energy in a sub-pulse is independent of its width, it could imply that the discharge process is operating at a maximum threshold level; in other words, once a series of sparks is initiated they probably extract a fixed (maximum) amount of energy from the vacuum gap. On the other hand, if the energy in a sub-pulse increases with increasing width, it might imply that the discharge process is operating at a level much lower than the maximum threshold; in other words, there is much more energy available than is usually extracted by the sparks, and more contiguous sparks imply more energy. Finally, if the energy in a sub-pulse decreases with increasing width, it might imply a high level of electric conductivity on the polar cap (transverse), which is not expected in normal pulsars due to the very huge magnetic fields, but may be plausible in ms pulsars. A further implication might be that the transverse development of the series of sparks on the polar cap (which is what the width essentially refers to) may or may not impede the vertical development of the sparks above the polar cap (which is what the energy essentially refers to). This may also be related to the competition of sub-pulse energies noticed in the drifting pulsar PSR B0031 -07 by Vivekanand & Joshi 1999. Such might be the kind of implications which might provide tight constraints on the details of the discharge of the vacuum gap.

That the spiky emission is almost absent from the third component of the integrated profile of PSR J0437-4715 further supports the special behavior of this component reported in Vivekanand et al 1998.

In principle, the shape of the integrated profiles of radio pulsars should be determined by the convolution of the distribution of sub-pulse positions with the distribution of sub-pulse energies, taking into account the shapes of sub-pulses, the random variations in them, etc. While mathematically there may be no further constraints on these two distributions, physically one would expect them to be simply related to the relevant component of the integrated profile. This is certainly not the case for the spiky emission in PSR J0437-4715. This raises questions such as, what exactly are the components of integrated profiles? Are they really individual beams of emission (Gil & Krawczyk 1997)? Is this picture justified in PSR J0437-4715 where the  $l$  emission is much wider than the components of the integrated profile? Clearly polarization data is an important independent input for this problem.

Another independent method of resolving the integrated profile into *independent*

*regions of emission on the polar cap* is proposed here. It assumes that the pulsar flux varies independently in each of these regions of emission. Then the cross-correlation of pulsar data at all pairs of phases (longitudes) within the integrated profile can be modeled, and optimized in terms of the minimum number of independent regions required for the model. To implement this, the pulsar data must show significant cross-correlation, which PSR J0437-4715 does. This is a difficult work and is currently in progress.

The main results of this paper are:

1. PSR J0437-4715 emits radio waves at 327 MHz on two time-scales: the (*s*) time-scale of  $\approx 0.026 \pm 0.001$  periods, that is much smaller than the widths of the components of the integrated profile, and the (*l*) time-scale that is much longer than the component widths (Table 1). The *s* emission occasionally takes place in the form of intense spikes.
2. The time-scale of the *s* emission is positively correlated with its relative contribution to the total radio emission in a given period. It is necessary to find out if the same occurs in normal pulsars also. This might constrain the details of discharge of vacuum gaps above pulsar polar caps.
3. The spiky emission in PSR J0437-4715 is confined to the main component of the integrated profile (component 2 in Figure 1) for 90% of the time, and to component 1 for the rest 10% of the time; it rarely occurs in component 3, which supports earlier claims of this component's special behavior (Vivekanand et al 1998).
4. The distribution of the positions of the spikes within a component of the integrated profile has no simple relation to the shape of that component. This raises questions concerning the meaning of the integrated profiles components in terms of independent regions of emission on the polar cap.

## References

1. Ables, J. G., McConnell, D., Deshpande, A. A. & Vivekanand, M. 1997, ApJ, 475, L33
2. Gil, J. & Krawczyk, A. 1997, MNRAS, 285, 561
3. Jenet, F. A., Anderson, S. B., Kaspi, V. M., Prince, T. A. & Unwin, S. C. 1998, ApJ, 498, 365
4. Kramer, M., Lange, C., Lorimer, D. R., Backer, D. C., Xilouris, K. M., Jessner, A. & Wielebinski, R. 1999, ApJ, 526, 957
5. Manchester, R. N. & Taylor, J. H. 1977, Pulsars, W. H. Freeman & Co.
6. McConnell, D., Ables, J. G., Bailes, M. & Erickson, W. C. 1996, MNRAS, 280 331
7. Navarro, J., Manchester, R. N., Sandhu, J. S., Kulkarni, S. R. & Bailes, M. 1997, ApJ, 486, 1019
8. Press, W. H. Flannery, B. P., Teukolsky, S. A. & Vetterling, W. T. 1989, Numerical Recipes (Cambridge: Cambridge Univ. Press)
9. Ruderman, M. A. & Sutherland, P. G. 1975, ApJ, 196, 51
10. Sallmen, S. & Backer, D. C. 1995, Astron. Soc. Pac. Conference Series, 72, 340
11. Vivekanand, M., Ables, J. G. & McConnell, D. 1998, ApJ, 501, 823
12. Vivekanand, M. & Joshi, B. C. 1999, Apj, 515, 398

Table 1. The first three columns contain the mean value of the width  $b$ , defined as  $\sum_{i=1}^{N_P} b_i/N_P$ , and its rms error defined as  $\sqrt{\sum_{i=1}^{N_P} [\sigma_{b_i}/N_P]^2}$ , for the three time-scales of radio emission. The four rows correspond to the four plots of Figure 4. For comparison, the widths of the three components of the integrated profile shown in Figure 1 (modeled as Gaussians) have been reproduced in the last column.

	$s$	$l$	$3$	
(a)	$0.0234 \pm 0.0023$	$0.2020 \pm 0.0061$	$0.2341 \pm 0.0475$	
(b)	$0.0255 \pm 0.0016$	$0.0995 \pm 0.0030$	$0.1080 \pm 0.0018$	0.078
(c)	$0.0271 \pm 0.0005$	$0.0611 \pm 0.0011$	$0.0684 \pm 0.0066$	0.051
(d)	$0.0263 \pm 0.0007$	$0.0561 \pm 0.0013$	$0.0596 \pm 0.0064$	0.044

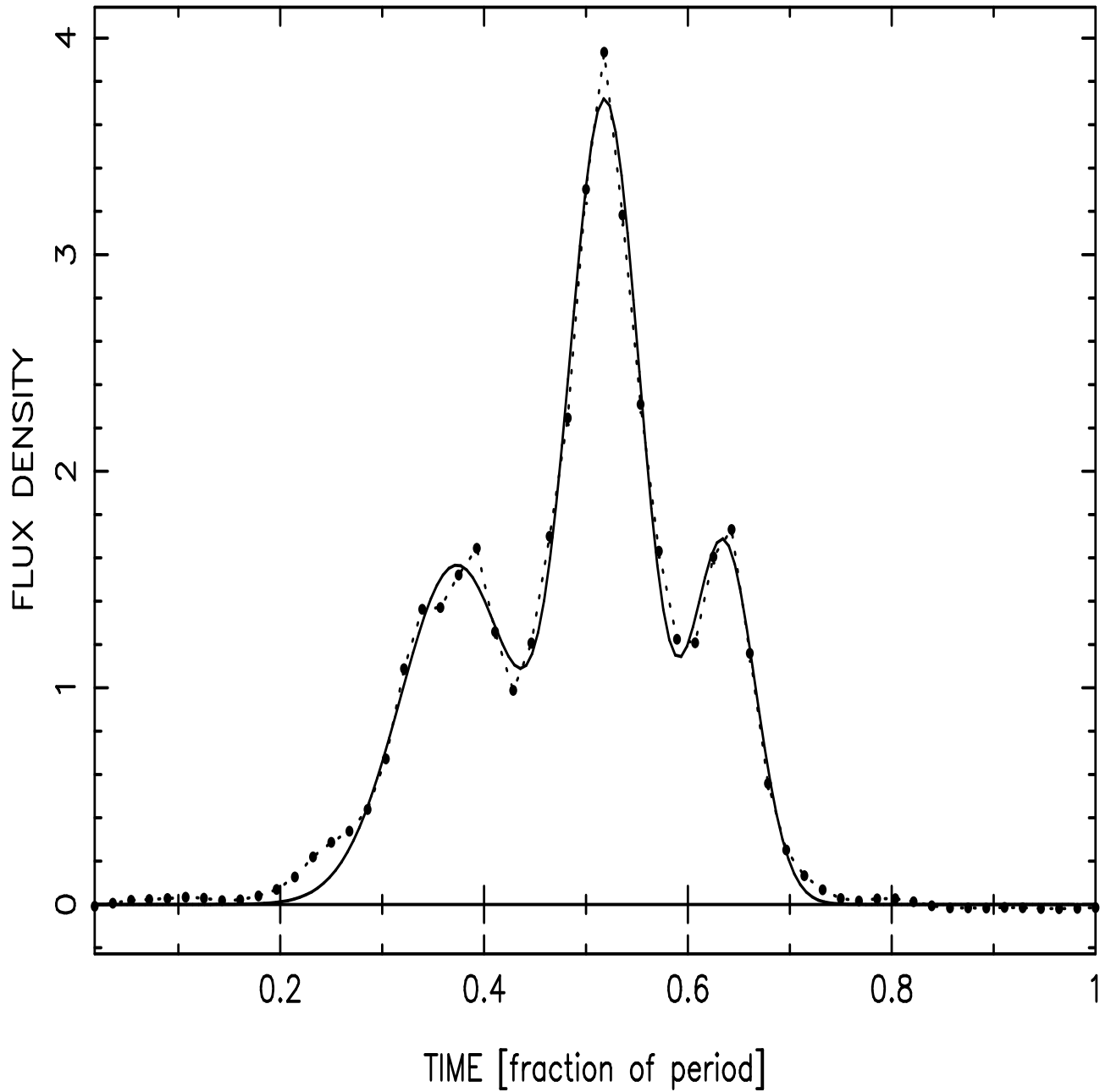


Fig. 1.— Integrated Profile of PSR J0437-4715 at 327 MHz using 436,500 periods (dots). The abscissa is time in units of the rotation period of PSR J0437-4715, while the ordinate is the flux density in arbitrary units. It has been resolved into three major components of emission, each represented by a Gaussian, whose sum is the smooth curve. The Gaussians are centered at 0.373, 0.519 and 0.635 periods, having widths 0.078, 0.051 and 0.044 periods, respectively. The abscissa is also known as the “phase” or “longitude” within the period.

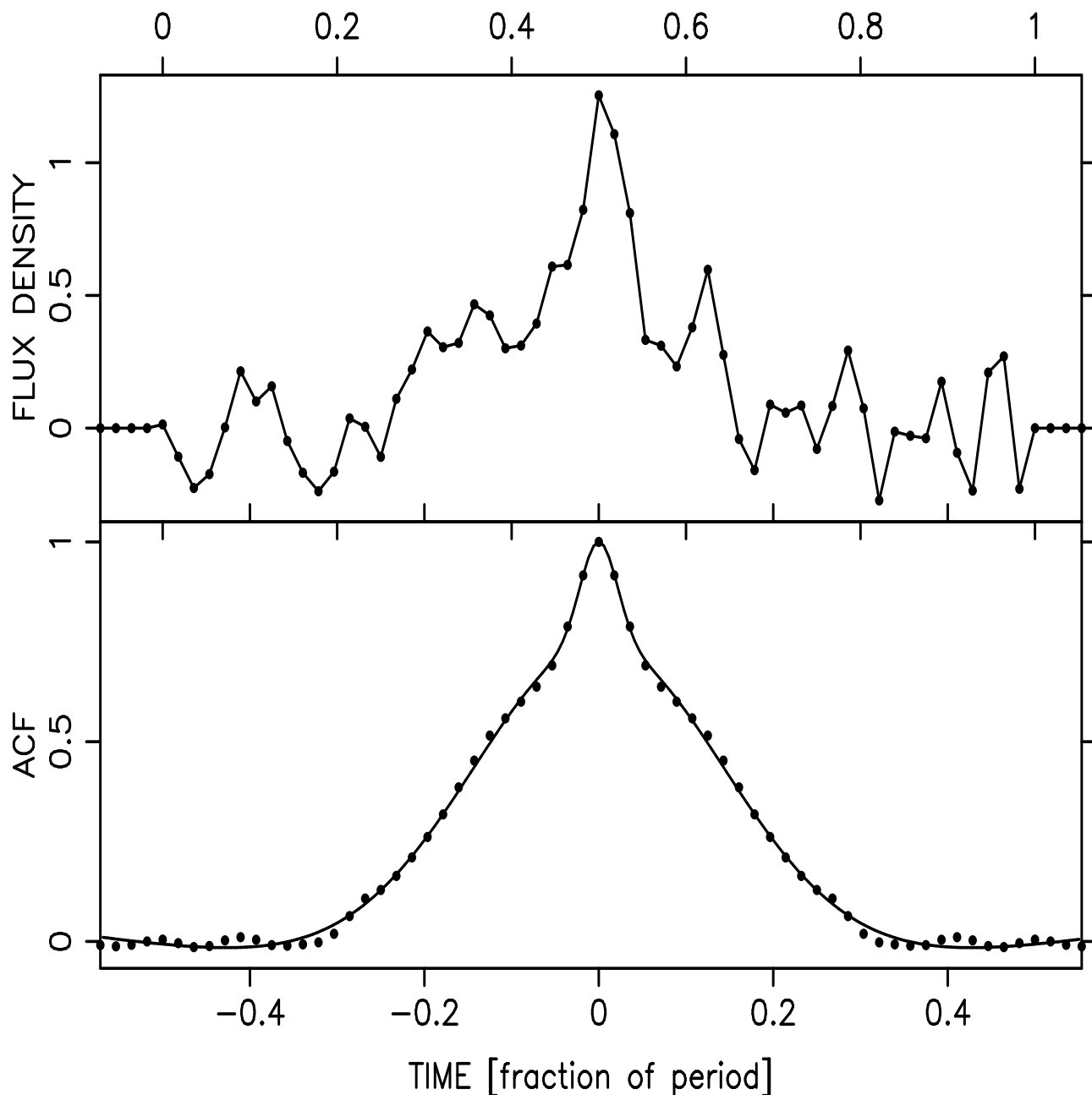


Fig. 2.— **Top frame:** Flux density (in arbitrary units) as a function of time (in fraction of period) for the 12<sup>th</sup> period in the data file observed on 1995 Mar 7 starting at 16:04:17 UT (observation code 50661604). The duration of the synthesized samples is 0.10281556 ms. The 56 samples of data are centered in an array of length 64 samples (for doing FFT). **Bottom frame:** The ACF of the data in the top frame, as a function of the time delay  $t$ . The dots represent the computed ACF, while the smooth curve is the best fit discussed in the text. The number of degrees of freedom is 32 (not 64) minus the number of parameters fit.



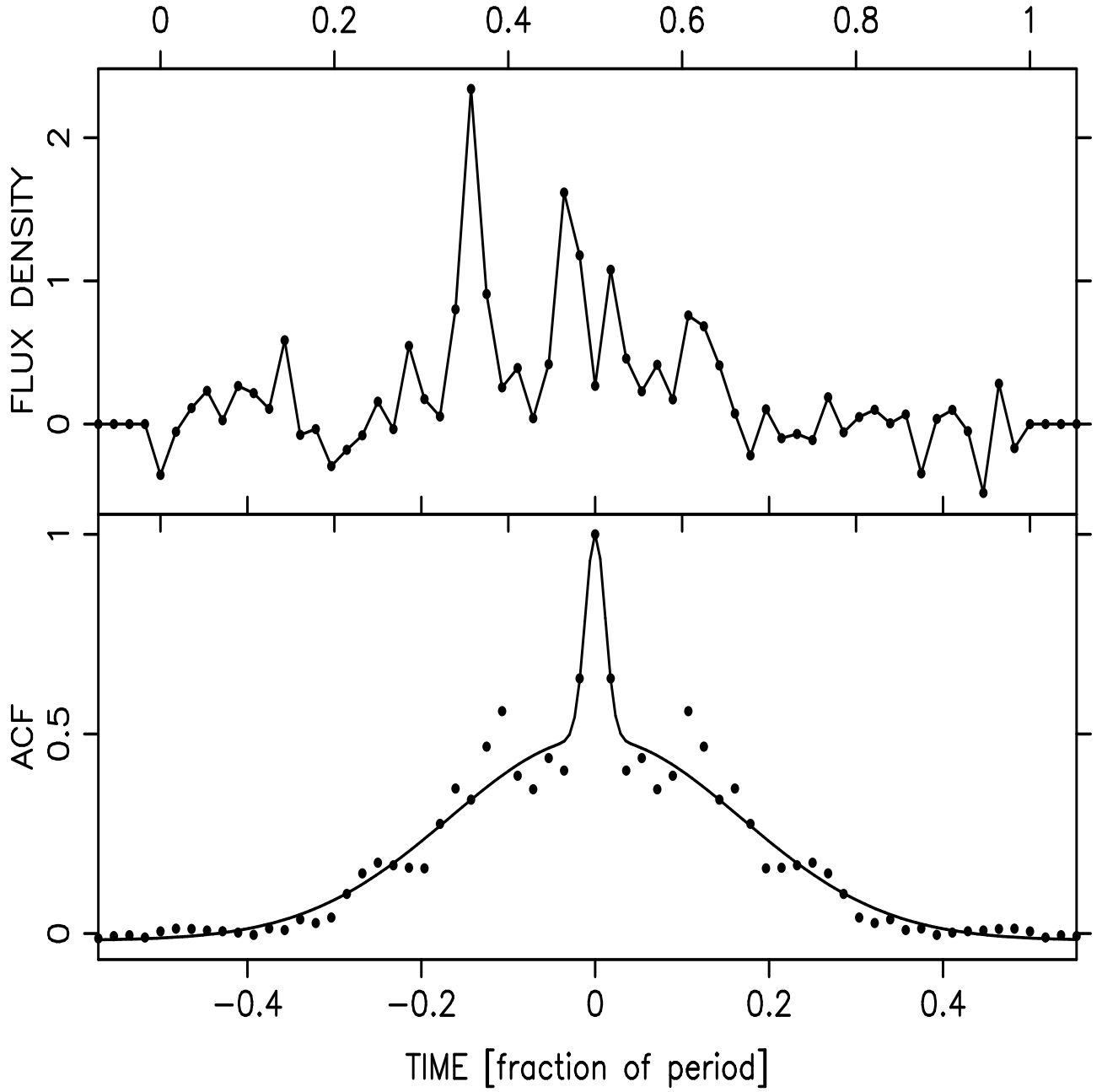


Fig. 3.— Same as in Figure 2, except that it is the 27<sup>th</sup> period of the same data file.

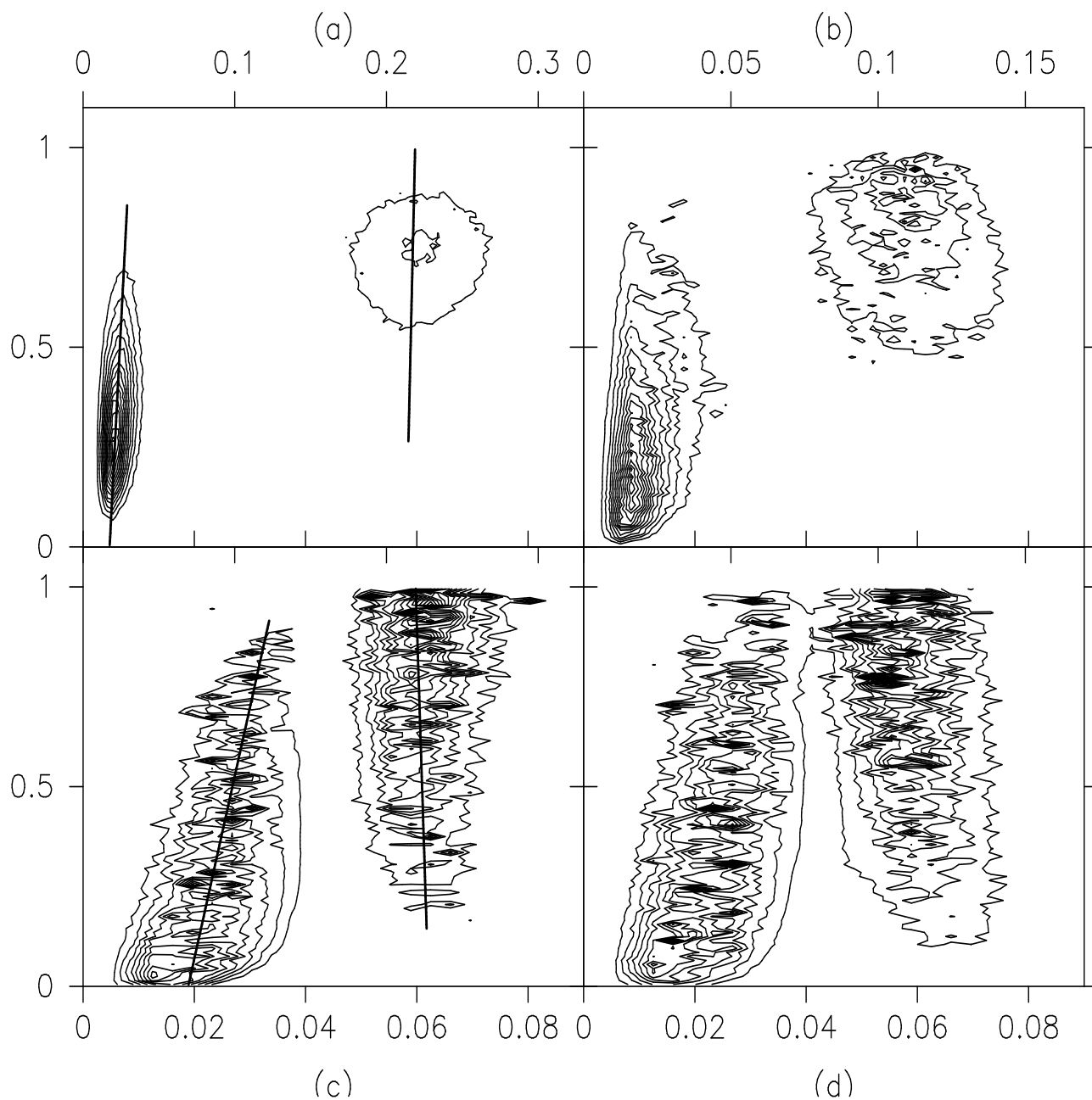


Fig. 4.— Contour plots of  $p(a, b)$  as a function of amplitudes  $a$  (ordinate) and widths  $b$  (abscissa) defined in equation 1. Plot (a) belongs to the entire integrated profile, while plots (b), (c) and (d) belong to the three components of the integrated profile defined in Figure 1, respectively. The total abscissa range (0.0 to 1.0 periods) and total ordinate range (0.0 to 1.0) were divided into 100 bins. The contours are 15 in number equally spaced in the  $p(a, b)$  space. The thick straight lines in plots (a) and (c) show the trend of the corresponding probability density in the  $a - b$  plot.

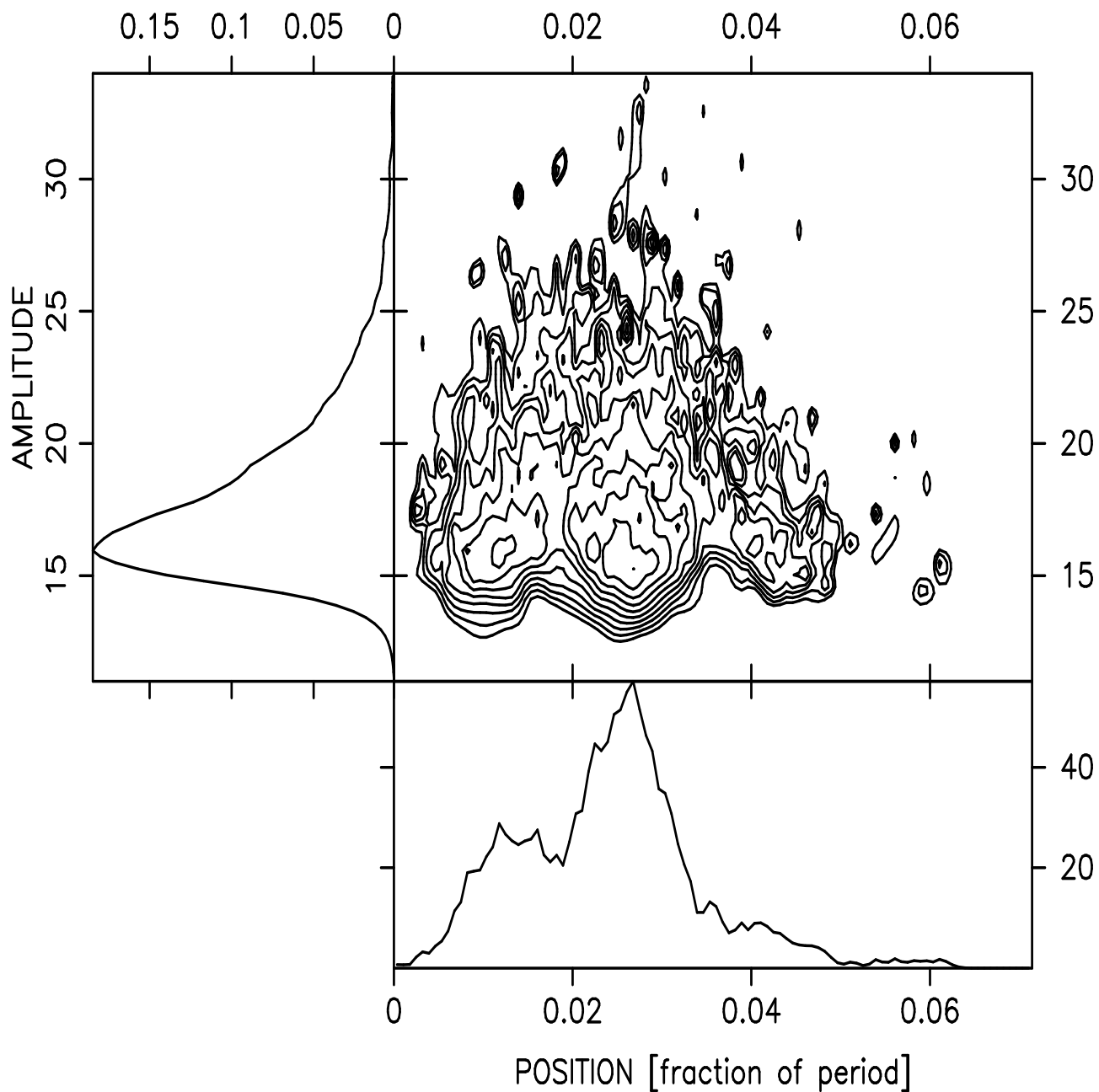


Fig. 5.— Probability density function of the peak flux density (ordinate) of the spikes versus their position (abscissa) in component 2 of the integrated profile shown in Figure 1. For reference the peak of component 2 lies at 0.027 on the abscissa. Fifteen contours are equally spaced in the logarithm of the probability. One dimensional probability distributions when the above plot is integrated horizontally and vertically are also shown. The threshold flux density for the most luminous data file was 10.0.

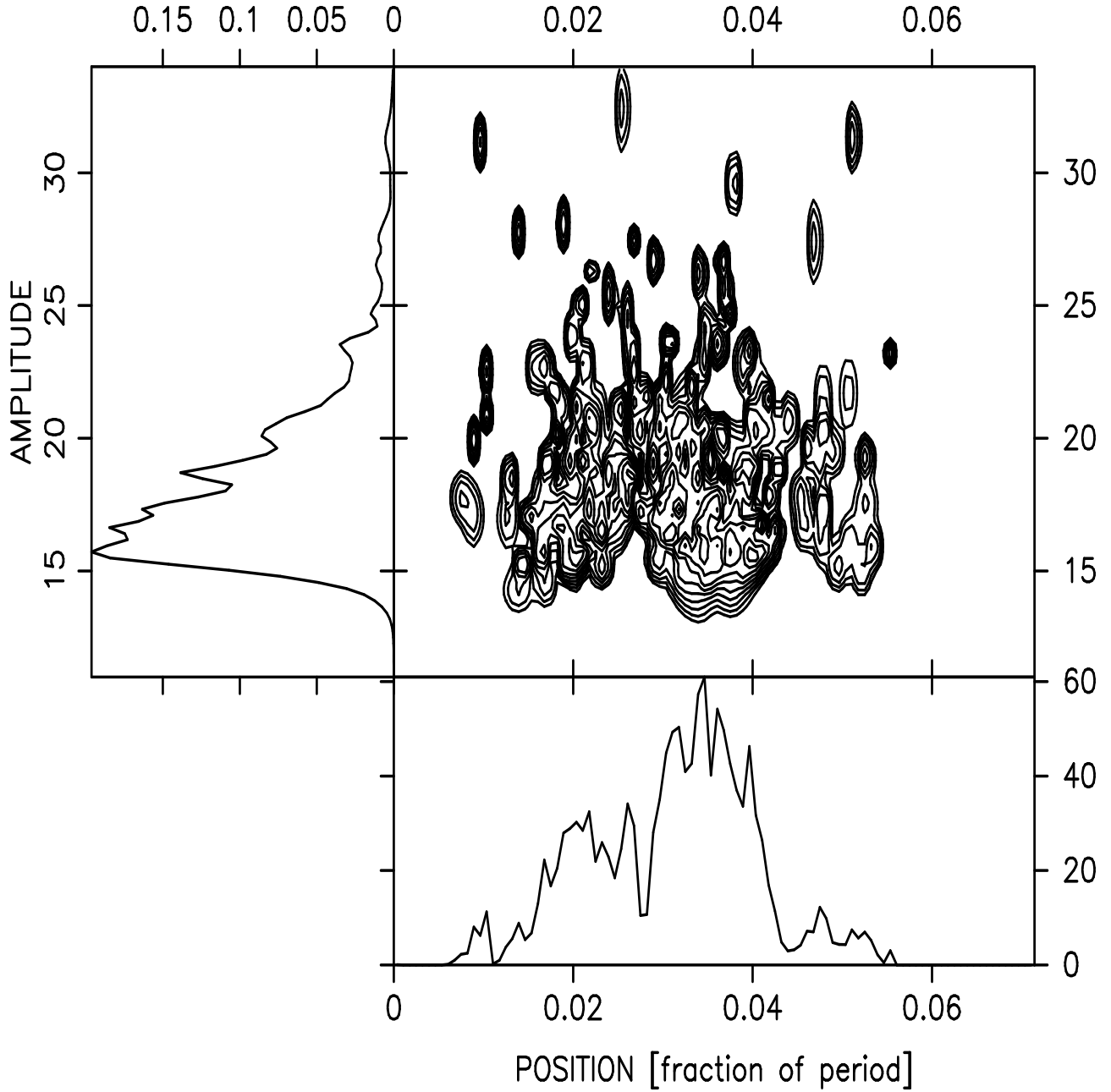


Fig. 6.— Same as in Figure 5, except that it refers to component 1 of the integrated profile shown in Figure 1. For reference the peak of component 1 lies at 0.036 on the abscissa.

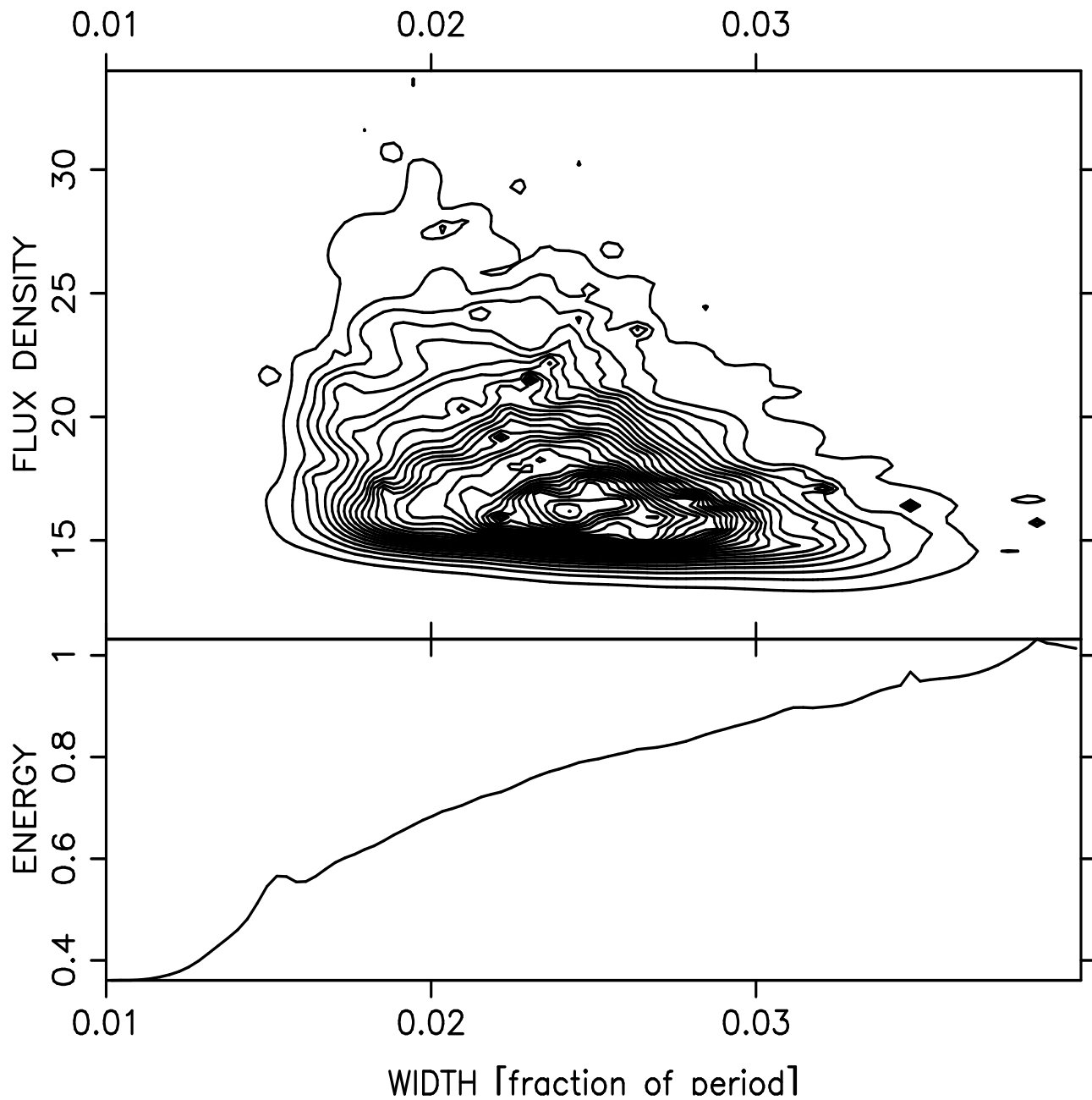


Fig. 7.— **Top frame:** Probability density function of the peak flux density (ordinate, in arbitrary units) of spikes versus their width (abscissa) in component 2 of the integrated profile shown in Figure 1. A single Gaussian was fit to the flux density of each spike. Twenty nine contours are equally spaced in the probability range. **Bottom frame:** The average energy in the spike (in arbitrary units), defined as  $\sqrt{\pi}$  times the peak flux density times the width, averaged along the ordinate at each value of the abscissa, as a function of the width.